applied sciences

MDPI

Article

Stability of Cu-Precipitates in Al-Cu Alloys

Torsten E. M. Staab [1,*,†], Paola Folegati [2,†], Iris Wolfertz [3] and Martti J. Puska [4]

1 LCTM, Universität Würzburg, Röntgenring 11, D-97070 Würzburg, Germany
2 Politecnico Milano, Polo di Como, Via Anzani 42, I-22100 Como, Italy; paola.folegati@polimi.it
3 HISKP, Universität Bonn, Nußallee 14-16, D-53115 Bonn, Germany; iris.wolfertz@hiskp.uni-bonn.de
4 Department of Applied Physics, Aalto University, P.O. Box 11100, FI-00076 Aalto, Finland; martti.puska@aalto.fi
* Correspondence: Torsten.Staab@uni-wuerzburg.de; Tel.: +49-931-31-81460
† These authors contributed equally to this work.

Received: 30 May 2018; Accepted: 9 June 2018; Published: 20 June 2018

Abstract: We present first principle calculations on formation and binding energies for Cu and Zn as solute atoms forming small clusters up to nine atoms in Al-Cu and Al-Zn alloys. We employ a density-functional approach implemented using projector-augmented waves and plane wave expansions. We find that some structures, in which Cu atoms are closely packed on {100}-planes, turn out to be extraordinary stable. We compare the results with existing numerical or experimental data when possible. We find that Cu atoms precipitating in the form of two-dimensional platelets on {100}-planes in the fcc aluminum are more stable than three-dimensional structures consisting of the same number of Cu-atoms. The preference turns out to be opposite for Zn in Al. Both observations are in agreement with experimental observations.

Keywords: aluminum copper alloys; Guinier-Preston zones; precipitates; ab initio calculations; DFT-LDA

1. Introduction

Al-Cu alloys have been under active scientific research and technological development for more than 100 years because of their applications in light weight constructions [1,2]. Nowadays, they are especially important in aviation and automotive industry. Aluminum alloys show a rich variety of metastable and stable phases from which a few are ordered compounds. Since usually the surface energy is too large to form directly thermodynamically stable phases, alloying elements precipitate in a sequence of clusters, zones and metastable phases. Clusters are non-ordered, locally increased concentrations of solute atoms, zones are locally ordered but do not have a long-range ordering, while stable and metastable phases possess the latter [3]. Zones and some metastable phases are typically fully coherent with the matrix [3].

Precipitation and clustering phenomena of solute atoms in a light metal matrix are the reason for the superior properties of aluminum alloys, i.e., this results in a high strength at a small specific weight. The obtained mechanical properties arise from a suitable thermal treatment of these alloys [2]. Typically, after casting these age hardenable alloys are extruded or rolled to their final form. Thereafter they undergo a solution heat treatment at about 100 . . . 150 K below the melting point of aluminum in order to obtain the maximum solubility of the chosen alloying elements [3]. After the heat treatment the materials are quenched to room temperature to freeze-in the finely distributed solute atoms. Storing these alloys then at room temperatures causes the solute atoms to diffuse by the help of quenched-in vacancies [4]. Via this process the solute atoms form agglomerates, which grow subsequently in size. After storing Al-Cu alloys for some hours at room temperature the agglomerates become visible in X-ray diffraction patterns and they are called Guinier-Preston zones according to

Guinier and Preston, who discovered them independently in 1938 [5–7]. Further storage at elevated temperature causes the growth of meta-stable Al-Cu phases: θ'' Al_3Cu and θ' Al_2Cu [3]. However, in new generation Al-Cu-Li alloys like AA2198, AA2050 or AA2199 besides Al-Cu-Li precipitates these Al-Cu-phases are detected as well [8,9]. Those Al-Cu-Li alloys are considered for the fuselage of new generation aircrafts due to their high strength and good welding behavior and have been, thus, subject to intense research in recent years (see e.g., [10,11]), while also Al-Cu alloys are still a matter of active research [12,13].

However, the understanding of the precipitation process in metallic alloys on the atomic level is still one of the main problems in materials science. It hampers a purposeful improvement of alloys, i.e., an alloy design as a bottom-up approach. Since the atomic structure of small, i.e., sub-nanometer, precipitates is difficult to access experimentally, numerical ab initio simulations are often the only way to obtain data on the geometry of atomic arrangements and their binding properties. Up to now, just a few numerical results on vacancy formation energies and di-vacancy binding energies in aluminum are available [14,15], which can be compared with accurate experimental data on vacancy formation energies in pure Al (see [16] for an overview). Only recently, research on vacancy binding with different isolated solute atoms has been published for Al [17,18] and Mg [19].

Results from ab initio calculations can be compared to experiments probing, e.g., vacancies by positron annihilation spectroscopy (PAS) [20–23] or individual elements by X-ray absorption [24,25] or small solute atom clusters employing the atom probe methods [26]. Moreover, the recently re-discovered X-ray absorption fine structure (XAFS) spectroscopy is sensitive for the atomic environment of, e.g., Cu-atoms [24,27]. For the two spectroscopic methods, PAS and XAFS, spectra can be calculated from first principles (For PAS see, e.g., ref. [28] and for XAFS [29]). The resulting spectra, which are related to trapping of positrons to vacancies or to the excitation of solute atoms like Cu and Zn by X-rays, depend strongly on the atomic positions around those defects. A comparison of the simulations with existing experimental data can be effectively used to search for an explanation of the clustering phenomena on the atomic level in different sample compositions and conditions. Thus, it can provide guidelines to metallurgists to perform thermal and mechanical treatments on Al-alloys in order to obtain the desired materials properties.

Specifically, the results of the present work clearly give an ab initio explanation, why in Al-Cu alloys copper precipitates on the $\{100\}$-planes, while for Al-Zn alloys three-dimensional (3D) agglomerates of Zn-atoms are formed. The reasons for these findings are easy to understand in the named simple two-component systems. However, his understanding will also pave the way for controlling processes taking place in actual technical alloys composed often of more than five elements.

The present paper is organized as follows. The computational schemes employed are presented in Section 2. Results on the formation energies of vacancies and di-vacancies are given in Section 3. Then we present vacancy-solute and solute-solute binding energies for clusters containing up to nine copper atoms. Section 4 contains a discussion – in particular, a comparison between the different employed calculation schemes is presented.

2. Methods: Computational Schemes

All our calculations are based on density functional theory (DFT) within the local density approximation (LDA). In some cases a comparison with the generalized gradient approximation (GGA) of DFT has been performed. The computations are carried out using the plane-wave code VASP [30,31], implemented with the projector augmented-wave (PAW) method to account for the valence electron-ion core interaction.

In our VASP calculations, we have employed supercells of different sizes—namely 64, 108, 128, 144 and 192 atoms per supercell are used to check the influence of finite size effects on the relaxation of the atoms and the derived total energies. In all calculations the first Brillouin zone of the superlattice is sampled using a Monkhorst-Pack (MP) **k**-point mesh [32]. Employing the 108-atom supercell for face-centered cubic (fcc) Al we compare the results obtained with $4 \times 4 \times 4$ and $6 \times 6 \times 6$ **k**-point

meshes to check the convergence of the total energy. Differences in the total energy of the systems are less than 5 meV per atom. All the calculations have thereafter been performed with the finer MP-mesh. A plane-wave cutoff of 300 eV is used in the calculation of the pseudo valence wave functions.

In the defect calculations, atomic positions are relaxed and the total energy is minimized until the forces acting on atoms are less than 0.04 eV/Å. The volume relaxation is not performed systematically, because we found that the use of a larger (108 and more atoms) supercells gives well-converged results without volume relaxation. However, results of test calculations employing the smallest (64 atom) supercell are given below. In the plane wave calculations we have used lattice constants optimized for each set of computational parameters, i.e., the cut-off energy and MP-mesh, used. For error cancellation, the total energy differences and relative ionic relaxations between defect and perfect bulk systems are calculated from results for supercells of the same size and obtained with the same computational parameters.

3. Results

3.1. Reliability of Modeling

To confirm the reliability of the employed numerical methods, we have calculated the formation energies (formation enthalpies at zero pressure) of mono- and di-vacancies in fcc Al. In the case of di-vacancies, we have considered nearest (1NN) and next nearest neighbor (2NN) configurations. The mono-vacancy formation energy is calculated as

$$H_{\mathrm{V}}^{\mathrm{F}} = E_{\mathrm{V(N-1)}} - \frac{N-1}{N} E_{\mathrm{Al_{bulk}}}(N) \tag{1}$$

where N is the number of atoms in the supercell, $E_{\mathrm{V(N-1)}}$ is the total energy of a fcc Al-supercell containing a mono-vacancy, and $E_{\mathrm{Al_{bulk}}}(N)$ is the total energy of a perfect fcc Al-supercell.

The formation energies obtained are given in Table 1. Our VASP calculations for the isolated mono-vacancy lead to values in close agreement with previous similar LDA calculations by Carling et al. [15] but also with a different approach like SIESTA [33] giving for the formation energy $H_{\mathrm{V}}^{\mathrm{F}} = 0.66$ eV [34,35]. All the calculated values deviated less than 0.05 eV from reliable experimental values [16]. Here, reference [16] is a summary of a few dozen experimental works, where the data are weighted according to their relevance by experts in the field. So, the given value of $H_{\mathrm{V}}^{\mathrm{F}} = 0.67$ eV for the vacancy formation energy in pure aluminum is an average of the most reliable values published.

Our results for the di-vacancy binding energies $H_{\mathrm{2V,X}}^{\mathrm{F}} - 2H_{\mathrm{V}}^{\mathrm{F}}$ (X = 1NN or 2NN) show that the interaction between nearest neighbor vacancies (X = 1NN) in Al is repulsive. This is in agreement with the results by Carling et al. [15] and also with the experimental finding that Al does not, in contrast to other metals like Cu [36,37], show a tendency for forming vacancy clusters after low-temperature irradiation and subsequent annealing [38]. However, the 2NN di-vacancy shows a tiny binding which is also in agreement with the results by Carling et al. [15].

Table 1. Comparison with experimental results: Formation energies for mono- $H_{\mathrm{V}}^{\mathrm{F}}$ and di-vacancies $H_{\mathrm{2V,X}}^{\mathrm{F}}$ in the nearest neighbor (X = 1NN) and next nearest neighbor (X = 2NN) positions in fcc Al. The binding energies $H_{\mathrm{2V,X}}^{\mathrm{b}}$ of the two vacancies in the two configurations are also given. Positive and negative binding energies indicate repulsion and binding, respectively. (SIESTA results: see [34]).

Method	Volume Relax	MP-Mesh	Atoms	$H_{\mathrm{V}}^{\mathrm{F}}$ (eV)	$H_{\mathrm{2V,1NN}}^{\mathrm{F}}$ (eV)	$H_{\mathrm{2V,2NN}}^{\mathrm{F}}$ (eV)	$H_{\mathrm{2V,1NN}}^{\mathrm{b}}$ (eV)	$H_{\mathrm{2V,2NN}}^{\mathrm{b}}$ (eV)
VASP-LDA	yes	$6 \times 6 \times 6$	64	0.71	—	—	—	—
VASP-LDA	no	$6 \times 6 \times 6$	64	0.713	1.506	1.409	+0.081	−0.016
VASP-LDA	no	$6 \times 6 \times 6$	108	0.714	1.489	1.421	+0.061	−0.007
VASP-GGA	no	$6 \times 6 \times 6$	108	0.66	—	—	—	—
SIESTA-DZP	no	$3 \times 3 \times 3$	108	0.64	—	—	—	—
Exp. [16]	—	—	—	0.67				

To further check the reliability of our calculations in terms of supercell sizes and **k**-point meshes, we have computed the solubility enthalpy of Cu in Al. It is calculated as

$$\Delta H_{\mathrm{mix}} = E_{\mathrm{CuinAl}} - \left[\frac{N-1}{N} E_{\mathrm{Al_{bulk}}} + \frac{1}{N} E_{\mathrm{Cu_{bulk}}} \right] \quad (2)$$

where E_{CuinAl} is the total energy of an fcc Al-supercell containing one Cu-atom, while $E_{\mathrm{Al_{bulk}}}$ and $E_{\mathrm{Cu_{bulk}}}$ are the total energies of pure fcc Cu- and Al-supercells, respectively. Supercells of the same size are used to calculate these energies. Note also that positive and negative values represent endothermic and exothermic reactions, respectively.

The numbers given in Table 2 are in agreement with the first-principles results by Wolverton et al. [17]. The small deviations indicate that, at least for single isolated Cu atoms, the energetics is well converged already for a supercell size of 108 atoms.

Table 2. Solubility enthalpy ΔH_{mix} of Cu in Al calculated by using Equation (2) and different supercell sizes.

Supercell Size (atom)	ΔH_{mix} (meV)
108	−50.5
128	−54.2
144	−53.0

3.2. Impurity-Cluster Binding Energies

The reliability of our calculations for Cu clusters is based on the tests described above. While for VASP the transferability of the pseudo potentials is well established, this is not the case for other methods. Especially, for SIESTA [33] the employed pseudo potentials have to be tested in well-known Al-Cu binding configurations of Al_2Cu as in ref. [34].

To begin with, we give in Table 3 the binding energies for a pair of Cu atoms with respect to two separate Cu atoms. These energies are obtained by optimizing the lattice constant for Al for each supercell size and **k**-point mesh. All the supercell sizes lead to a binding energy of around 50 meV. For the 128 atom supercell the binding energy is the smallest one reflecting the small spacing between the adjacent Cu habit planes of the periodic images and the ensuing artificial interaction.

Table 3. Binding energy of two Cu solute atoms in Al on nearest neigbor positions in fcc Al. The c-direction is perpendicular to the habit plane of the Cu atoms. Negative signs indicate binding.

Scheme	Number Atoms	Size Unit Cells	k-points	E_{bind} (meV)
LDA	108	$3 \times 3 \times 3$	$4 \times 4 \times 4$	−50.3
LDA	128	$4 \times 4 \times 2$	$4 \times 4 \times 8$	−46.3
LDA	144	$3 \times 3 \times 4$	$4 \times 4 \times 4$	−56.2
LDA	192	$4 \times 4 \times 3$	$3 \times 3 \times 6$	−54.7
GGA	108	$3 \times 3 \times 3$	$6 \times 6 \times 6$	−51.5

We will give the total binding energies of two- (2D) and three-dimensional (3D) copper clusters as the energy gain relative to separated Cu atoms in aluminum. From this we calculate the binding energy also per Cu-atom, i.e., the average over the cluster. We calculate also the binding energy of the last Cu-atom attached to a cluster, which indicates, if it is energetically favorable for an already existing cluster to grow further by attaching another Cu atom. This energy has to be compared to the thermal energy at room temperature of $3/2\,\mathrm{k}T = 40\,\mathrm{meV}$. The construction scheme of the 2D Cu-platelets on the {100}-plane of the fcc Al-lattice is shown in Figure 1. It is based on well-established experimental facts on Cu-platelet formation [3,5,6,39].

Firstly, we have performed calculations on small agglomerates up to 4 Cu atoms. The results are presented in Table 4. We observe that two Cu-atoms on the 1NN positions are bound together with a binding energy of about 50 meV, while there is a weak binding of 2NN Cu-atoms of about 10 meV

as well. However, the most important result is that 2D agglomerates of 4 Cu on the {100}-plane of the fcc Al are preferred instead of the 3D tetrahedron structure (h) with an energy difference of 259 meV for the triangle configuration (g) and with 398 meV for the rectangle configuration (f) in Table 4 (cf. also Figure 1).

Table 4. Binding energies for agglomerates of Cu atoms in 1D, 2D, and 3D configurations. The calculation employed the 108 atom supercell. Given is the total binding energy, the binding energy per Cu-atom, and the binding energy of the 'last' Cu atom specified in Figure 1. We give here the energy with an accuracy of 0.1 meV, which is only of internal numerical relevance. The numbering is according to Figure 1 left.

Agglomerate	**atom no.**	**Spatial**	E_{bind} **(meV)**	E_{bind} **(meV)**	E_{bind} **(meV)**
structure		extension	cluster	per Cu	last Cu
(a) 2 Cu 1NN on (100)-plane	1, 2	2D	−50.3	−25.1	−50.2
(b) 2 Cu 2NN on (100)-plane	1, 4	2D	−9.6	−4.8	−9.6
(c) 3 Cu in-line on (100)-plane	6, 7, 8	1D	−95.2	−31.7	−45.0
(d) 3 Cu triangle on (100)-plane	1, 2, 3	2D	−134.7	−44.9	−84.4
(e) 3 Cu triangle on (111)-plane	–	2D	− 97.4	−32.5	−47.1
(f) 4 Cu rectangle on (100)-plane	1, 2, 3, 4	2D	−344.7	−86.2	−210.0
(g) 4 Cu triangle on (100)-plane	1, 2, 3, 5	2D	−206.1	−51.5	−71.4
(h) 4 Cu tetrahedron in space	–	3D	+53.0	+13.2	+150.4

Experimentally, there is, since the early investigations by Guinier and Preston [5,6] a long-standing agreement on the fact that Cu prefers to precipitate as 2D platelets on the {100}-planes of the fcc Al [40,41] . Recently, this has been even confirmed by HR-TEM [39] showing mono-atomic platelets on the three equivalent {100}-planes in the fcc lattice. Our results presented in Table 4 confirm this perception. Of the triangular structures (d) and (e) the platelet structure (d) in the (100)-plane is favored by nearly 40 meV compared to the platelet structure (e) on a (111)-plane. However, the close-packed structure (h) of Cu-atoms in the form of a 3D tetrahedron even shows repulsion. Please note that larger Cu-platelets ((f) in Table 4) show the largest binding per Cu-atoms, i.e., they are the most stable ones.

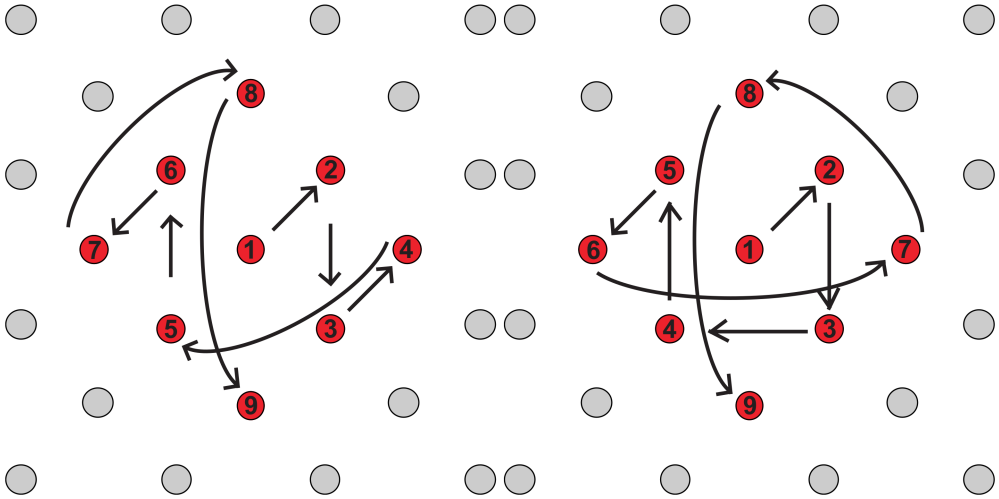

Figure 1. Configuration of Cu-atoms in 2D platelets on the {100}-plane in fcc Al. The Cu and Al atoms are shown by red and grey spheres, respectively. The numbering indicates how the Cu-platelets were assumed to grow. The left and right patterns show the sequences 1 and 2 used in the calculations, respectively.

3.2.1. 2D-Cu-Clusters in 108-atom Supercells

Having confirmed the preference for copper to precipitate as platelets on the {100}-planes in fcc aluminnum, we have constructed larger platelets starting from the two different 4-Cu-atom configurations (f) and (g) in Table 4 and using the sequences 1 and 2 in Figure 1, respectively. The numbering gives the order, in which the Cu-atoms have been attached to the Cu-platelet. All calculations have been performed in the LDA scheme using a MP-mesh given in Table 5.

The binding energy of the last Cu atom to a cluster of $N-1$ atoms is shown in the left graph of Figure 2, where $n=2$ corresponds to the Cu-atom pair on 1NN positions. The way of constructing the Cu-platelets is shown in Figure 1. From Figure 2 it is evident that the triangular structure of four Cu atoms (sequence 2) is much less favorable than the square one (sequence 1). This means that once the quite stable triangle has formed, the forth copper atom attaching is likely to complete the small triangle rather to a square (sequence 1) than forming a larger triangle (sequence 2). This is also reflected in the higher binding energy per Cu atom shown in the right graph of Figure 2. Attaching the 7th, 8th, or 9th atom does not make a difference between the sequences due to their symmetry.

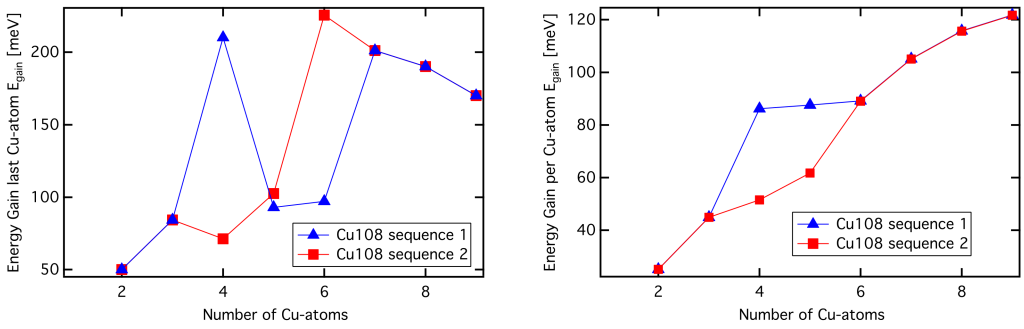

Figure 2. Energy gain during Cu-cluster growth for a supercell of 108 atoms in sequences 1 and 2. (**left**) The energy gain due to the last attached Cu atom, (**right**) the total energy gain per Cu atom in the growing cluster. Sequences 1 and 2 are explained in Figure 1.

Table 5. Used supercells with corresponding MP-meshes.

Type	Size (atoms)	Size (Unit Cell)	MP-mesh
standard	108	$3\times3\times3$	$4\times4\times4$
flattened	128	$4\times4\times2$	$4\times4\times6$
elevated	144	$3\times3\times4$	$3\times3\times2$
widened	192	$4\times4\times3$	$2\times2\times3$

The right part of Figure 2 shows the energy gain per copper atom for platelets consisting of 4- and 5-atom in sequence 1 in comparison to sequence 2. This significant increase is caused by relaxations perpendicular to the habit plane of the Cu atoms.

3.2.2. 2D-Cu-Clusters in 128- and 192-atom Supercells

Lattice relaxations within the habit plane of the Cu-platelet cause an interaction between neighboring supercells. Hence, a 108-atom supercell ($3\times3\times3$ unit cells) is already quite small to accommodate a Cu-platelet consisting of more than 5 atoms. Thus, we have repeated some of the calculations in enlarged supercells to keep the growing platelets farther apart from each other between the periodic images of the supercells.

On the one hand, we employed a supercell of 128 atoms ($4\times4\times2$ unit cells) increasing the lateral distance of the periodic images, while reducing the distance perpendicular to the platelets in the $<001>$-direction. On the other hand, a supercell of 192 atoms ($4\times4\times3$ unit cells) increases the

lateral distance while keeping the distance in between Cu-platelets in the $< 001 >$-direction the same as for the 108-atoms cell (cf. Table 5). The results for these supercells are shown in Figures 3 and 4.

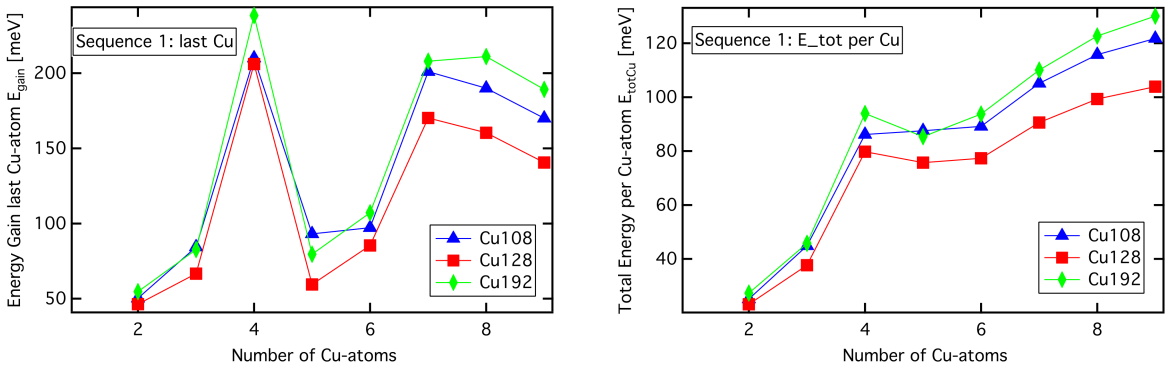

Figure 3. Energy gain during Cu-cluster growth. Results corresponding to supercells of 108, 128, and 192 atoms are compared. (**left**) Energy gain due to the last Cu atom attached, and (**right**) total energy gain per Cu-atom of a growing cluster. Sequence 1 is explained in Figure 1.

For the flattened supercell of 128 atoms (see Table 5) the separation between the copper platelets in the habit plane increases compared to the supercell of 108 atoms, while the distance between the platelets and their periodic images becomes obviously too small. Figures 3 and 4 show that the energy gain by relaxation is significantly smaller for the supercell of 128 atoms, which artificially suppresses the energy-lowering relaxation perpendicular to the platelets (see Figure 5).

The use of the supercell of 144 atoms, on the other hand, just increases the separation perpendicular to the copper platelets (see Table 5). Thus, the size of the platelets has to be limited to five Cu atoms and therefore this configuration is not considered further. Finally, the use of the supercell of 192-atoms (4×4 lattice constants wide, but three lattice constants in height as well) reduces the interactions between copper platelets in the habit plane, while the separation of the platelets in the $< 001 >$-direction is the same as for the supercell of 108 atoms. Thus, this supercell gives the largest energy gain as seen from Figures 3 and 4.

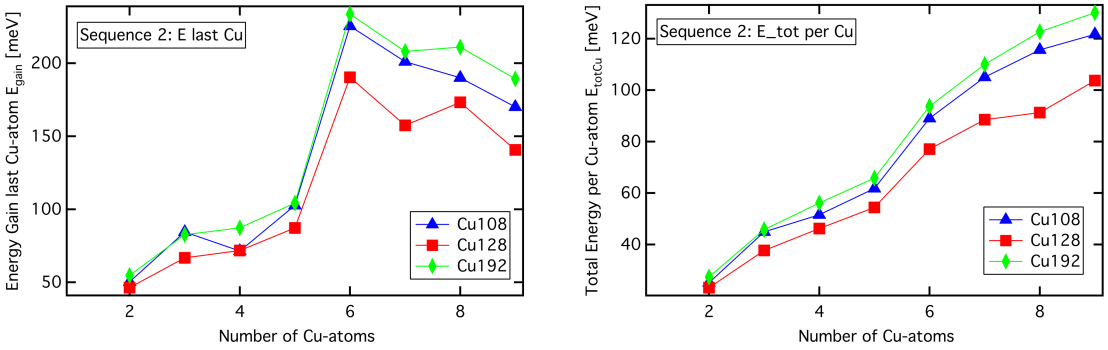

Figure 4. Energy gain during Cu-cluster growth. The results corresponding to the supercells of 108, 128, and 192 atoms are compared. (**left**) Energy gain of the last Cu atom attached, (**right**) total energy gain per Cu-atom of a growing cluster. Sequence 2 is explained in Figure 1.

Since the energy differences are nevertheless small, i.e., less than 10% between the supercells of 108 and 192 atoms, we have chosen the computationally more feasible supercell of 108 atoms for the following discussion.

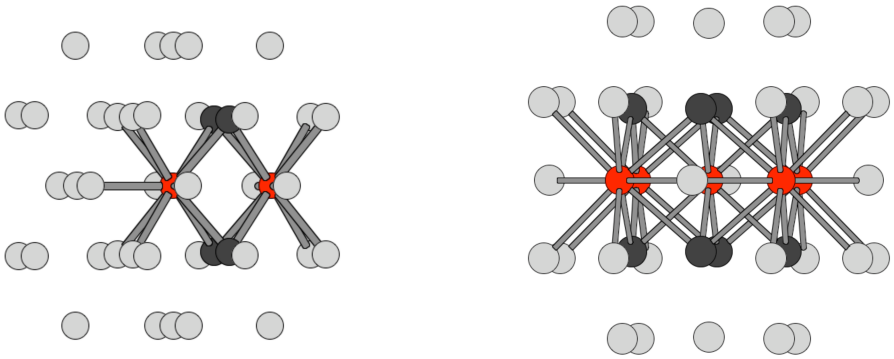

Figure 5. Relaxation patterns of growing clusters. (**left**) Two copper atoms (red spheres) on 1NN position, (**right**) five Cu-atoms arranged as a platelet on the {100}-plane. The Al atoms having two or more bonds to Cu-atoms are plotted in dark-grey color. The relaxation of the Al-layer above and below towards the Cu-atoms on the {100}-plane clearly increases with the number of agglomerated Cu-aotms.

3.2.3. Lattice Relaxations

As shown in Figure 5, the relaxation of the Al-layers above and below a copper platelet, residing on the {100}-plane, clearly increases with the number of agglomerated copper atoms. For a platelet consisting of five Cu atoms the aluminum layers relax towards the copper platelet by about 20 pm or 10% compared to the ideal separation of lattice planes (202 pm). This is a similar behavior as observed numerically for 5-atomic copper platelets [34] or experimentally [5,40,41] for GP-I zones, which are described as a single extended layer of Cu atoms on a {100}-plane (see [3]).

3.2.4. Relaxed Versus Static Configurations

To clarify the role of the strong relaxation around the Cu atoms in the aluminum lattice on the observed energy gain, we compare static (atoms fixed at their ideal aluminium lattice positions) and relaxed atomic configurations. Figure 6 shows the results for a supercell of 108 atoms and for 2D and 3D configurations. Even though the unrelaxed case is unphysical, it gives already the major contribution to the energy gain in forming Cu-platelets. We can also conclude that the energy gain due to relaxation of the surrounding Al atoms is more important than the exact shape of the precipitate.

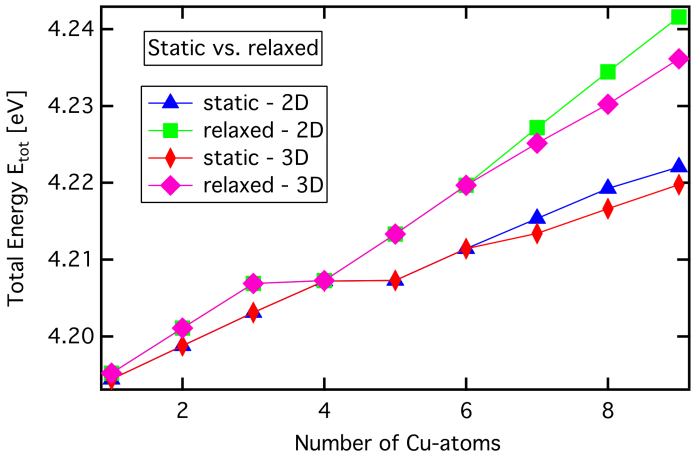

Figure 6. Total energies calculated by using static (atoms fixed) and relaxed configurations of a supercell of 108 atoms.

3.2.5. Comparison with Zinc Clusters

In contrast to copper, which has an fcc structure, zinc crystalizes in a hexagonal closed-packed (hcp) lattice. Our calculations show that there is a binding energy between the 1NN Zn-atoms. However, it is clearly smaller than in the case of copper—i.e., only around 20 meV. The binding energies of Zn atom clusters in different 2D platelet and 3D configurations are given in Figure 7. In the 3D configuration with five Zn atoms the binding energy is around 24 meV/Zn atom whereas in the 2D configuration it is only around 14 meV/Zn atom. This preference to form 3D precipitates is in contrast to the behavior of Cu precipitates and it reflects the different lattice structures of copper and zinc resulting in the tendency of Zn to form spherical precipitates [42–45].

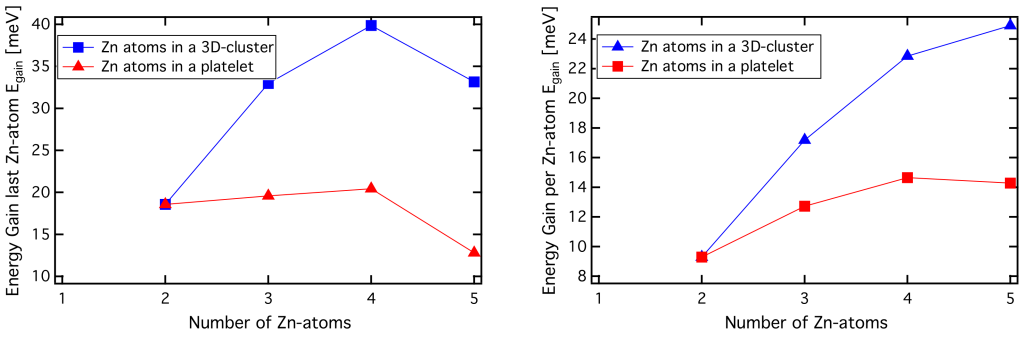

Figure 7. Binding energies of Zn atoms in 2D and 3D Zn clusters. (**left**) The binding energy for the last attached Zn atom. (**right**) The binding energy per Zn atom in the cluster.

3.2.6. Pre-Guinier-Preston Zones in Al-Cu and Al-Zn

The small energetically-favored 2D Cu precipitates on the Al {100}-planes, shown schematically in Figure 1 or with relaxed atomic positions in Figure 5, can be considered to be the starting point of growing Guinier-Preston zones. Guinier-Preston zones become visible in XRD when they have reached a size of about 1–1.4 nm [41], i.e., consisting of more than 24–48 atoms. A size of 1.4 nm may be still too small for visibility in the TEM or HR-TEM. However, due to the computational limitations we could consider here only platelets of the maximal number of nine atoms.

Due to the experimental fact that detects in as-quenched pure Al-Cu alloys show positron lifetimes, which should be related to an open volume of about a mono-vacancy in Al [4,46] one can assume that—at least some—GP zones must contain structural vacancies. Some structures of Cu-platelets containing vacancies have been calculated by SIESTA in ref. [34].

4. Discussion and Conclusions

Our computational results employing DFT-LDA are consistent and in sufficient agreement with previously calculated and experimental values. Especially, our results on vacancies in aluminum agree well with other ab initio calculations [15] and experiments [16] giving credence to our approach. Moreover, the inward relaxation of nearest-neighbor Al-atoms surrounding a single Cu atom is in accordance with experimental results from X-ray absorption [47]. Furthermore, we find a binding between Cu atoms situated on the {100}-habit planes in fcc aluminum, while, e.g., a 3D tetrahedron even shows a repulsive interaction. Thus, 2D structures are favored compared to 3D ones, which is in agreement with experimental observations finding mono-atomic copper platelet on the {100}-planes in the fcc Al-lattice when segregation of the super saturated solution is starting [41].

The calculated total energies for a 2D copper cluster vary slightly with used supercell sizes and shapes. However, the dependence of the total energy on the number of Cu atoms shows a similar trend in all cases. Nevertheless, it turns out that there have to be at least three layers of Al atoms in the supercell perpendicular to the Cu-habit plane separating periodic images of the copper platelets. Obviously, the relaxation of aluminum planes parallel to the copper platelet, which is important for

energy lowering, cannot be reliably described with wide but flat supercells. This type of cells is not large enough in the z-direction perpendicular to the copper platelet.

In contrast to magic number arrangement of defects in semiconductors [48], for metallic materials it seems to be difficult to state that distinguished structures are existing at all. While in general the binding energies for different geometric configurations differ very little (about 50–100 meV), we also find some special platelet structures of Cu atoms with quite high binding energies between the copper species. However, the generally small differences in binding energies may be responsible for not finding any special configurations in experiments. Remarkable is only that some closed configurations of Cu atoms on the {100}-planes show higher binding energies per Cu atom (four Cu arranged in a square). Obviously, their geometries allow electronic structures, which are energetically more favorable. However, it seems to be experimentally demanding to confirm this finding.

Concerning 3D instead of 2D plate-like structures, such as the 3D-tetrahedron, we find that these close-packed structures are the least favorable ones at all, since the Cu atoms inside their habit plane have a tendency to move away from each other. Hence, close-packed 3D-structures are unlikely to be energetically favorable in Al-Cu alloys.

According to our calculations the formation of platelets during the aging of Al-Cu alloys is in contrast to Al-Zn alloys, where obviously 3D-Clusters are preferred. Again, this is in accordance with experimental results for pure Al-Zn alloys, where clusters grow in early stages of decomposition in a spherical manner [41,43,45].

Author Contributions: Conceptualization, P.F. and M.J.P. and T.E.M.S.; Methodology, P.F. and M.J.P.; Software, P.F.; Validation, P.F. and M.J.P. and T.E.M.S.; Formal Analysis, P.F. and T.E.M.S.; Investigation, P.F.; Resources, P.F.; Data Curation, P.F.; Writing Original Draft Preparation, P.F. and T.E.M.S.; Writing Review & Editing, M.J.P. and I.W.; Visualization, T.E.M.S.; Supervision, M.J.P.; Project Administration, M.J.P. and T.E.M.S.; Funding Acquisition, P.F. and T.E.M.S.

Funding: This research was funded in part by the German Research Foundation (Deutsche Forschungsgemeinschaft—DFG) grant number STA 527/3-2 and STA 527/5-1. This publication was funded by the German Research Foundation (DFG) and the University of Wuerzburg in the funding programme Open Access Publishing.

Acknowledgments: We acknowledge large computational resources provided by Politecnico di Milano on the clusters Avogadro.

Conflicts of Interest: The authors declare no conflict of interest. The founding sponsors had no role in the design of the study; in the collection, analyses, or interpretation of data; in the writing of the manuscript, and in the decision to publish the results.

Abbreviations

The following abbreviations are used in this manuscript:

PAS	Positron Annihilation Spectroscopy
XAFS	X-ray Absorption Fine Structure
DFT	Density Functional Theory
LDA	Local Density Approximation
GGA	General Gradient Approximation
VASP	Vienna Ab initio Simulation Package
PAW	Projector Augmented Wave
MP	Monkhorst-Pack
SIESTA	Spanish Initiative for Electronic Simulations with Thousands of Atoms
DZP	Double Zeta Polarized
1NN	Nearest Neighbors
2NN	Next Nearest Neighbors
XRD	X-Ray Diffraction
TEM	Transmission Electron Microscopy
HR-TEM	High resolution Transmission Electron Microscopy
fcc	face-centered cubic
hcp	hexagonal closed-packed

References

1. Polmear, I. *Light Alloys—From Traditional Alloys to Nanocrystals*, 4th ed.; Elsevier: Amsterdam, The Netherlands, 2006.
2. Ostermann, F. *Anwendungstechnologie Aluminium*, 3rd ed.; Springer: Berlin/Heidelberg, Germany, 2014.
3. Haasen, P. *Physical Metallurgy*, 3rd ed.; Cambridge University Press: Cambridge, UK, 1996.
4. Dupasquier, A.; Folegati, P.; de Diego, N.; Somoza, A. Current positron studies of structural modifications in age-hardenable metallic systems. *J. Phys. Condens. Matter* **1998**, *10*, 10409–10422. [CrossRef]
5. Guinier, A. La diffraction de rayon X aux tres petis angles: Application a l'etude de phenomenes ultramicroscopiques. *Ann. Phys.* **1938**, *12*, 161–237.
6. Preston, G. The Diffraction of X-Rays by an Age-Hardening Aluminum and Copper Alloys. *Proc. R. Soc. Lond. Ser. A Math. Phys. Sci.* **1938**, *167*, 526–538. [CrossRef]
7. Preston, G. The Diffraction of X-Rays by an Age-Hardening Alloy of Aluminum and Copper: The Structure of an Intermediate Phase. *Lond. Edinb. Dublin Philos. Mag. J. Sci.* **1938**, *26*, 855–871. [CrossRef]
8. De Geuser, F.; Bley, F.; Denquin, A.; Deschamps, A. Mapping the microstructure of a friction-stir welded (FSW) Al-Li-Cu alloy. *J. Phys.: Conf. Ser.* **2010**, *247*, 012034. [CrossRef]
9. De Geuser, F.; Bley, F.; Deschamps, A. A new method for evaluating the size of plate-like precipitates by small-angle scattering. *J. Appl. Cryst.* **2012**, *45*, 1208–1218. [CrossRef]
10. Decreus, B.; Deschamps, A.; Donnadieu, P.; Ehrström, J.C. On the Role of Microstructure in Governing Fracture Behavior of an Aluminum-Copper-Lithium Alloy. *Mater. Sci. Eng. A* **2013**, *586*, 418–427. [CrossRef]
11. Le Jolu, T.; Morgeneyer, T.; Denquin, A.; Sennour, M.; Laurent, A.; Besson, J.; Ourgues-Lorenzon, A.F. Microstructural Characterization of Internal Welding Defects and their Effect on the Tensile Behaviour of FSW Joints of AA2198 Al-Cu-Li Alloy. *Metall. Mater. Trans. A* **2014**, *45A*, 5531–5544. [CrossRef]
12. Bourgeois, L.; Dwyer, C.; Weyland, M.; Nie, J.F.; Muddle, B. Structure and Energetics of the Coherent Interface between the Θ′ Precipitate Phase and Aluminium in Al-Cu. *Acta Mater.* **2011**, *59*, 7043–7050. [CrossRef]
13. Zhang, Y.; Zhang, Z.; Medhekar, N.; Bourgeois, L. Vacancy-tuned Precipitation Pathways in Al-1.7 Cu-0.025In-0.025Sb (at.%) Alloy. *Acta Mater.* **2017**, *141*, 341–351. [CrossRef]
14. Carling, K.; Wahnström, G.; Mattsson, T.; Sandberg, N.; Grimvall, G. Vacancy Concentration in Al from Combined first-principles and Model Potential Calculations. *Phys. Rev.* **2003**, *B67*, 054101. [CrossRef]
15. Carling, K.; Wahnström, G.; Mattsson, T.; Mattsson, A.; Sandberg, N.; Grimvall, G. Vacancies in Metals: From first-principles Calculations to Experimental Data. *Phys. Rev. Lett.* **2000**, *85*, 3862–3865. [CrossRef] [PubMed]
16. Ullmaier, H. (Ed.) *Landolt-Börnstein—Numerical Data and Functional Relationships in Science and Technology—New Series—Group III: Crystal and Solid State Physics Volume 25: Atomic Defects in Metals*; Springer: Berlin, Germany, 1991.
17. Wolverton, C.; Ozoliņš, V. First-principles Aluminum Database: Energetics of Binary Al Alloys and Compounds. *Phys. Rev.* **2006**, *B73*, 144104. [CrossRef]
18. Wolverton, C. Solute-Vacancy Binding in Aluminum. *Acta Mater.* **2007**, *55*, 5867–5872. [CrossRef]
19. Shin, D.; Wolverton, C. First-principles Study of Solute-Vacancy Binding in Magnesium. *Acta Mater.* **2010**, *58*, 531–540. [CrossRef]
20. Haaks, M.; Staab, T. High Momentum Analysis in Doppler Spectroscopy. *Appl. Surf. Sci.* **2008**, *255*, 84–88. [CrossRef]
21. Klobes, B.; Staab, T.; Haaks, M.; Maier, K.; Wieler, I. The Role of Quenched-in Vacancies for the Decomposition of Aluminium Alloys. *Phys. Status Solidi (RRL) Rapid Res. Lett.* **2008**, *2*, 224–226. [CrossRef]
22. Klobes, B.; Korff, B.; Balarisi, O.; Eich, P.; Haaks, M.; Maier, K.; Sottong, R.; Hühne, S.M.; Mader, W.; Staab, T. Probing the Defect State of Individual Precipitates Grown in an Al-Mg-Si Alloy. *Phys. Rev.* **2010**, *B82*, 054113. [CrossRef]
23. Klobes, B.; Maier, K.; Staab, T. Natural Ageing of Al-Cu-Mg Revisited from a Local Perspective. *Mater. Sci. Eng. A* **2011**, *528*, 3253–3260. [CrossRef]

24. Klobes, B.; Staab, T.; Dudzik, E. Early Stages of Decomposition in Al Alloys Investigated by X-Ray Absorption. *Phys. Status Solidi (RRL) Rapid Res. Lett.* **2008**, *2*, 182–184. [CrossRef]
25. Klobes, B.; Korff, B.; Balarisi, O.; Eich, P.; Haaks, M.; Kohlbach, I.; Maier, K.; Sotong, R.; Staab, T. Defect Investigations of Micron Sized Precipitations in Al Alloys. *J. Phys. Conf. Ser.* **2011**, *262*, 012030. [CrossRef]
26. Wang, S.; Starink, M. Precipitations and Intermetallic Phases in Precipitation Hardening Al-Cu-Mg-(Li) Based Alloys. *Int. Mater. Rev.* **2005**, *50*, 193–215. [CrossRef]
27. Staab, T.; Zamponi, C.; Haaks, M.; Modrow, H.; Maier, K. Atomic Structure of pre-Guinier-Preston Zones in Al-Alloys. *Phys. Status Solidi (RRL) Rapid Res. Lett.* **2007**, *1*, 172–174. [CrossRef]
28. Makkonen, I.; Hakala, M.; Puska, M. Calculation of Valence Electron Momentum Densities using the Projector Augmented-Wave Method. *J. Phys. Chem. Solids* **2005**, *66*, 1128–1135. [CrossRef]
29. Rehr, J.; Albers, R. Theoretical Approaches to X-Ray Absorption Fine Structure. *Rev. Mod. Phys.* **2000**, *72*, 621–654. [CrossRef]
30. Kresse, G.; Furthmüller, J. Efficiency of *ab initio* Total Energy Calculations for Metals and Semiconductors using a Plane-Wave Basis Set. *Comput. Mater. Sci.* **1993**, *6*, 15–50. [CrossRef]
31. Kresse, G.; Furthmüller, J. Efficient Iterative Schemes for *ab initio* Total-Energy Calculations using a Plane-Wave Basis Set. *Phys. Rev.* **1996**, *B54*, 11169–11186. [CrossRef]
32. Monkhorst, H.; Pack, J. Special Points for Brillouin-Zone Integrations. *Phys. Rev.* **1976**, *B13*, 5188–5192. [CrossRef]
33. Soler, J.; Artacho, E.; Gale, J.; García, A.; Junquera, J.; Ordejón, P.; Sánchez-Portal, D. The SIESTA Method for ab initio Order-N Materials Simulation. *J. Phys. Condens. Matter* **2002**, *14*, 2745–2779. [CrossRef]
34. Kohlbach, I.; Korff, B.; Staab, T. (Meta-) Stable Phases and Pre-Guinier-Preston Zones in AlCu-Alloys Constructed from ab initio Relaxed Atomic Positions—Comparison to Experimental Methods. *Phys. Status Solidi B* **2010**, *247*, 2168–2178. [CrossRef]
35. Wolfertz, I. Ab initio Untersuchungen an frühen Ausscheidungsphasen der Aluminium(-Magnesium-) Kupfer-Legierungen. Ph.D. Thesis, HISKP, University Bonn, Bonn, Germany, 2014.
36. Mantl, S.; Triftshäuser, W. Defect Annealing Studies on Metals by Positron Annihilation and Electrical Resistivity Measurements. *Phys. Rev.* **1978**, *B17*, 1645–1652. [CrossRef]
37. Staab, T.; Krause-Rehberg, R.; Vetter, B.; Kieback, B. The influence of Microstructure on the Sintering Process in Crystalline Metal Powders investigated by Positron Lifetime Spectroscopy: Part I: Electrolytic and Spherical Copper Powder. *J. Phys. Condens. Matter* **1999**, *11*, 1757–1786. [CrossRef]
38. Rajainmäki, H.; Linderoth, S. Stage II Recovery in Proton-Irradiated Aluminum Studied by Positrons. *J. Phys. Condens. Matter* **1990**, *2*, 6623–6630. [CrossRef]
39. Konno, T.; Kawasaki, M.; Hiragi, K. Characterization of Guinier-Preston Zones by High-Angle Annular Detector Dark-Field Scanning Transmission Electron Microscopy. *JEOL News* **2001**, *36E*, 14–17.
40. Hardy, H. Report on Precipitation. *Prog. Met. Phys.* **1954**, *5*, 143–278. [CrossRef]
41. Baur, R.; Gerold, V. Entmischungsvorgänge im System Aluminium-Kupfer. *Zeitschrift für Metallkunde* **1966**, *57*, 181–186.
42. Gerold, V.; Schweizer, W. Die Kinetik von Entmischungsvorgängen in übersättigten Aluminium-Zink-Mischkristallen. *Zeitschrift für Metallkunde* **1961**, *52*, 76–86.
43. Gerold, V. Die Zonenbildung in Aluminium-Zink-Legierungen. *Phys. Status Solidi A* **1961**, *1*, 37–49. [CrossRef]
44. Dlubek, G.; Kabisch, O.; Brümmer, O.; Löffler, H. Precipitation and Dissolution Processes in Age-Hardenable Al Alloys—A Comparison of Positron Annihilation and X-Ray Small Angle Scattering Investigations—I. Al-Zn(x) (x = 3, 4.5, 6, 10, 18 at.%). *Phys. Status Solidi A* **1979**, *55*, 509–518. [CrossRef]
45. Krause, R.; Dlubek, G.; Wendrock, G. Structural Changes during Post-Ageing of an Al-Zn (15 at.%) Alloy at 100°C Studied by Positron Annihilation, Small Angle X-Ray Scattering and Microhardness Measurements. *Cryst. Res. Technol.* **1985**, *20*, 1495–1501. [CrossRef]
46. Gläser, U.; Dlubek, G.; Krause, R. Vacancies and Precipitates in Al—1.9 at % Cu Studied by Positrons. *Phys. Status Solidi A* **1991**, *163*, 337–343. [CrossRef]

47. Fontaine, A.; Lagarde, P.; Naudon, A.; Raoux, D.; Spanjaard, D. EXAFS Studies on Al-Cu Alloys. *Philos. Mag. B* **1979**, *40*, 17–30. [CrossRef]
48. Staab, T.; Haugk, M.; Frauenheim, T.; Leipner, H. Magic Number Vacancy Clusters in GaAs—Structure and Positron Lifetime Studies. *Phys. Rev. Lett.* **1999**, *83*, 5519–5522. [CrossRef]